Detection of Tropical Deep Convective Clouds from AMSU-B Water Vapor Channels Measurements

Gang Hong and Georg Heygster

Institute of Environmental Physics, University of Bremen, Bremen, Germany

Jungang Miao

Electromagnetics Laboratory, Baihang University, Beijing, China

Klaus Kunzi

Institute of Environmental Physics, University of Bremen, Bremen, Germany

Submitted to J. Geophys. Res. Atmospheres, April 2004.

Gang Hong, Institute of Environmental Physics, University of Bremen, Post Box 330440, Bremen 28334, Germany. (honggang@uni-bremen.de)

Georg Heygster and Klaus Kunzi, Institute of Environmental Physics, University of Bremen, Post Box 330440, Bremen 28334, Germany.

Jungang Miao, Electromagnetics Laboratory, Baihang University, Beijing 100083, China.

Abstract. Methods to detect deep convective clouds and convective overshooting from measurements at the three water vapor channels (183.3 ± 1, 183.3 ± 3, and 183.3 ± 7 GHz) of the Advanced Microwave Sounder Unit (AMSU)-B are presented. Thresholds for the brightness temperature differences between the three channels are suggested as criterion to detect deep convective clouds, and an order relation between the differences is used to detect convective overshooting. The procedure is based on an investigation of the influence of deep convective cloud systems on the microwave brightness temperatures at frequencies from 89 to 220 GHz using the simultaneous aircraft microwave and radar measurements over two tropical deep convective cloud systems, taken during the Tropical Rainfall Measuring Mission (TRMM) Large Scale Biosphere-Atmosphere Experiment (LBA) campaign. Furthermore, a microwave radiative transfer model and simulated mature tropical squall line data derived from the Goddard Cumulus Ensemble (GCE) model are used to adapt the criteria to the varying viewing angle of AMSU-B. These methods are employed to investigate the distributions of deep convective clouds and convective overshooting in the tropics (30°S to 30°N) for the four three-month seasons from March 2002 to February 2003. The distributions show a seasonal variability of shifting from the winter hemisphere to the summer hemisphere. The distributions of deep convective clouds follow the seasonal patterns of the surface rainfall rates. The deep convective clouds over land penetrate more frequently into the tropical tropopause layer than those over ocean. The averaged deep convective cloud fraction is about

0.3% in the tropics and convective overshooting contributes about 22% to this.

1. Introduction

Deep convective clouds comprise about $40-45\%$ of total cloud signals in the Intertropical Convergence Zone (ITCZ) [*Gu and Zhang*, 2002]. They play a major role in Earth's climate by transporting Earth's heat, moisture, and momentum from lower to upper troposphere. The tropical tropopause layer (TTL) between about $14-18$ km [e.g. *Sherwood and Dessler*, 2000, 2001; *Alcala and Dessler*, 2002], is the important transition layer between the convectively dominated tropical troposphere and the radiatively controlled stratosphere [e.g. *Highwood and Hoskins*, 1998; *Sherwood and Dessler*, 2000; *Thuburn and Craig*, 2002], that accounts for much of the air entering the stratosphere from troposphere. Thus deep convective clouds penetrating the TTL affect the exchange of air between the troposphere and the stratosphere, and thereby influence the physical and chemical processes occurring in the TTL and the stratosphere [e.g. *Lelieveld and Crutzen*, 1994; *Holton et al.*, 1995; *Thompson et al.*, 1997; *Sherwood and Dessler*, 2001; *Dessler*, 2002; *Gettelman et al.*, 2002; *Andronache et al.*, 2002].

Observations [e.g. *Thompson et al.*, 1997; *Gettelman et al.*, 2002] and model simulations [e.g. *Thompson et al.*, 1997; *Di Giuseppe and Tompkins*, 2003] have helped to understand the influence of deep convective clouds on the physical and chemical processes occurring in the TTL and the stratosphere. A critical prerequisite for this is the quantification of the frequencies, heights, and locations of deep convective clouds [*Alcala and Dessler*, 2002]. Because of the lack of ground-based cloud observations over oceans, satellite data including passive measurements of visible, infrared, and microwave radiances and active

measurements of radar have been used in the studies of deep convective clouds [e.g. *Liu et al.*, 1995; *Hall and Haar*, 1999; *Gettelman et al.*, 2002; *Alcala and Dessler*, 2002].

Methods to identify tropical deep convective clouds using infrared measurements are generally based on thresholds of cloud top temperatures, which have been defined with different values [*Mapes and Houze*, 1993]; for example, -65°C by *Hall and Haar* [1999], -58°C by *Fu et al.* [1990] and *Gettelman et al.* [2002], -43°C by *Hendon and Woodberry* [1993], and $-40°$ by *Liu et al.* [1995]. Different temperature thresholds result in detecting more or less deep convective clouds. *Mace et al.* [2001] and *Luo et al.* [2003] defined that thin cirrus cloud by top temperatures less than -35°C. The cirrostratus and cirrocumulus fractions are tightly connected with deep convective cloud fractions [*Chou and Neelin*, 1999]. Thus, it is difficult to distinguish deep convective clouds and cirrus clouds if only the methods based on infrared temperature thresholds are used. *Liu et al.* [1995] distinguished thin high cirrus clouds and deep convective clouds in terms of cloud top temperatures derived from infrared measurements and a microwave index defined by brightness temperatures at frequencies of 19.35 and 85.5 GHz of the Special Sensor Microwave/Imager (SSM/I). However, the method of *Liu et al.* [1995] is a rainfall retrieval scheme. Their classification is intended to maximize correlations in the retrieved rainfall while the validity for cloud type was not checked [*Anagnostou and Kummerow*, 1997; *Hong et al.*, 1999]. A convective and stratiform classification scheme independent of any rainfall retrieval scheme using SSM/I 85 GHz brightness temperature observations was developed by *Anagnostou and Kummerow* [1997]. *Hong et al.* [1999] improved it using higher resolution microwave observations of the Tropical Rainfall Measuring Mission (TRMM) Microwave Imager (TMI). However, the schemes of *Anagnostou and Kummerow*

[1997] and *Hong et al.* [1999] only classify convective and stratiform clouds, whereas deep convective clouds are still undistinguished from the convective clouds.

With high accuracy and excellent space and time resolutions, radar systems can provide direct measurements of the structure of clouds. Before the launch of TRMM in 1997, groundbased [e.g. *Heymsfield and Fulton*, 1988; *Cifelli et al.*, 2002], shipborne [e.g. *DeMott and Rutledge*, 1998; *Rickenbach and Rutledge*, 1998], and airborne [e.g. *Heymsfield et al.*, 1996; *Geerts et al.*, 2000] radar systems were used to observe the vertical structure and microphysical characteristics of deep convective clouds. Some of these investigations showed deep convective clouds penetrating into the TTL. However, as documented by *Alcala and Dessler* [2002], these measurements were confined to local geographic regions to study individual cloud systems and were not able to provide observations of deep convective clouds over a global scale. Since the launch of TRMM, the TRMM Precipitation Radar (PR), the first satellite-borne radar, can provide three dimensional cloud structure over a global scale enabling more accurate observations of deep convective cloud systems than before. The vertical structure of deep convective cloud systems using the PR has been documented widely [*Simpson et al.*, 1998; *Nesbitt et al.*, 2000; *Cecil et al.*, 2002; *Toracinta et al.*, 2002; *Alcala and Dessler*, 2002; *Kelley and Stout*, 2004]. *Alcala and Dessler* [2002] used the PR to identify and characterize deep convection extending into the TTL over the entire tropics. They found that the amount of overshooting convection is about 5% of total deep convective cloud and about 1.5% of the total convective rain area. The detailed vertical structure of convective towers in tropical cyclone eyewalls was studied by *Kelley and Stout* [2004] using the PR from 1998 to 2001. Convective systems evolve on time scales less than one day and are organized on space scales of the orders of

100 km [*Hendon and Woodberry*, 1993]. Although the PR has high vertical (0.25 km at nadir) and horizontal (4.3 km at nadir) resolutions, the swath of the PR (215 km wide prior to the 2001 boost and 250 km wide afterward) is too narrow to see the entire large scale cloud systems [*Kelley and Stout*, 2004]. The narrow swath of the PR and the long TRMM satellite return period (four to five days) result in difficulties to monitor short lived convective clouds.

The Advance Microwave Sounding Unit (AMSU)-B series onboard NOAA-15, 16, and 17 have been used to observe tropical cyclones [e.g. *Kidder et al.*, 2000], precipitation [e.g. *Staelin and Chen*, 2000; *Bennartz et al.*, 2002; *Chen and Staelin*, 2003, 2004], and clouds [e.g. *Zhao and Weng*, 2002; *Weng et al.*, 2003] using the advantages of their wide swaths (about 2200 km) and wide frequency range of their microwave channels ($89 - 190$ GHz). The key advantage of the AMSU-B channels is the unique ability to penetrate clouds [e.g. *Burns et al.*, 1997; *Greenwald and Christoper*, 2002]. However, the atmosphere is not entirely transparent at these frequencies in cases where thick clouds or precipitation significantly contaminate the sounder's field of view [*Eyre*, 1990]. The effects of clouds and precipitation on microwave radiances at the AMSU-B channels have been examined through simulations [e.g. *Muller et al.*, 1994; *Burns et al.*, 1997; *Skofronick-Jackson et al.*, 2002; *Bennartz and Bauer*, 2003] and observations [e.g. *Wang et al.*, 1997, 1998; *Greenwald and Christoper*, 2002]. The presence of hydrometeors in the upper levels of clouds with high cloud top results in large brightness temperature depressions at the AMSU-B frequencies above 150 GHz. Furthermore, for the three channels near to the water vapor absorption line centered at 183.3 GHz (183.3 ± 1, ± 3, ± 7 GHz), the farther is the frequency from the center, the larger is the brightness temperature depression [*Burns et al.*,

1997]. This is because the 183.3 ± 7 GHz channel can view deeper into clouds than the other two water vapor channels. The temperature weighting functions of the three water vapor channels maximize at different altitudes and they are above 9 km for precipitating clouds [*Burns et al.*, 1997]. Their different responses suggest a potential to delineate the distributions of hydrometeors above 10 km in clouds [*Burns et al.*, 1997; *Wang et al.*, 1997, 1998]. A criterion based on the difference between measured brightness temperatures at 183.3 ± 3 and 183.3 ± 1 GHz was suggested to screen out convective clouds before water vapor retrieval by *Burns et al.* [1997].

The present study derives methods for detecting deep convective clouds and convective overshooting in the tropics using satellite measurements at the AMSU-B water vapor channels. In section 2, *in situ* measurements of aircraft radar and microwave radiances are used to analyze the effects of deep convective cloud systems on microwave brightness temperatures at frequencies from 89 to 220 GHz, so as to suggest the criteria for detecting deep convective clouds and convective overshooting. The criteria are confirmed by simulated microwave radiances over a tropical squall line system in section 3. The criteria take into account the variation of the viewing angle of AMSU-B over the swath. In section 4, our methods are applied to one year of AMSU-B data to determine seasonal means of deep convective cloud fractions and convective overshooting fractions in the tropics. The results are compared with the TRMM rainfall products of the same periods.

2. Detection of Deep Convective Clouds from Aircraft Microwave and Radar Observations

2.1. Aircraft Microwave and Radar Data

The TRMM Large Scale Biosphere-Atmosphere Experiment (LBA) was carried out in southwestern Amazonia from 1 November 1998 to 28 February 1999. The main focus of the experiment was on the dynamical, microphysical, electrical and adiabatic heating characteristics of tropical convective systems. The observations during the TRMM LBA with a variety of instruments have been used to analyze mesoscale convective systems [*Cifelli et al.*, 2002]. Two deep convective cloud systems observed on 25 January and 10 February 1999 are chosen in our study because there were simultaneous measurements from the ER-2 Doppler radar (EDOP) and the Millimeter-wave Imaging Radiometer (MIR) onboard the ER-2 aircraft flying at an altitude of 20 km. The EDOP radar is a dual-beam Doppler weather radar at X-band (9.6 GHz) with a nadir footprint of 1 km. Its vertical resolution is 37.5 m, the horizontal resolution along the track is about 100 m [*Heymsfield et al.*, 1996]. The EDOP radar data can provide information on vertical hydrometeor structure, including the melting layer, the convective core locations and heights [*Heymsfield et al.*, 1996]. The MIR is a cross-track scanning radiometer that measures radiation at frequencies of 89, 150, 183.3 ± 1, 183.3 ± 3, 183.3 ± 7, 220, and 340 GHz. It scans in a plane perpendicular to the direction of flight with a swath of $\pm 50^\circ$ from nadir, which results in a ground swath of about 42 km at its cruising altitude of about 20 km for all frequencies. The radiometric measurement accuracy of the MIR is better than 1 K in the brightness temperature range of $240 - 330$ K, and about $2 - 4$ K for brightness temperatures below 100 K. Because the EDOP radar does not sample off nadir directions, only the MIR measurements at nadir are used in this section. The fairly straight flight tracks from 11.84°S,

61.98°W to 12.46°S, 61.79°W (time is from 2217:30 (hhmm:ss) to 2223:22 UTC, distance is about 75 km) and from 10.83°S, 61.88°W to 10.54°S, 62.01°W (time is from 1813:24 to 1816:14 UTC, distance is about 37 km) are taken for the deep convective cloud systems.

2.2. Effects of Deep Convective Clouds on Brightness Temperatures at the AMSU-B Channels

Although effects of deep convective clouds on brightness temperatures at the AMSU-B channels have been investigated by simulations [e.g. *Burns et al.*, 1997; *Wang et al.*, 1997] and observations [e.g. *Heymsfield et al.*, 1996; *Burns et al.*, 1997; *Wang et al.*, 1997, 1998], these studies are primarily focussed on understanding the effects of precipitation and clouds on brightness temperatures. *Heymsfield et al.* [1996] suggested a possible classification of the clouds and the precipitation according to convective cores, elevated ice layers, and rain without significant ice above the melting layer using brightness temperature differences between 150 and 220 GHz, 89 and 220 GHz, and 37 and 86 GHz, respectively. *Wang et al.* [1997] primarily investigated the effects of storms on the microwave radiances at water vapor channels of 183.3 ± 1, 183.3 ± 3, and 183.3 ± 7 GHz. They found an analogy between brightness temperatures at these channels over the storm-associated scattering media and those over a dry atmosphere with a cold ground. Similar results were documented by *Burns et al.* [1997] who suggested a criterion to screen out intense oceanic convection using the brightness temperature difference between 183.3 ± 3 and 183.3 ± 1 GHz. This work starts with analyzing the effects of deep convective clouds on brightness temperatures at the AMSU-B channels, especially at the three water vapor channels. However, unlike the aforementioned work, we focus on finding methods

to detect deep convective clouds and convective overshooting from measurements at the AMSU-B water vapor channels.

Figure 1 shows the collocated observed data in the flight track of 2217:30 to 2223:22 UTC on 25 January 1999, including the MIR observed brightness temperatures at frequencies between 89 and 220 GHz, the observed brightness temperature differences between 183.3± 1 and 183.3 ± 7 (ΔT_{17}) , 183.3 ± 1 and 183.3 ± 3 (ΔT_{13}) , and 183.3 ± 3 and 183.3 ± 7 GHz (ΔT_{37}), and the EDOP radar reflectivities. The EDOP radar reflectivities (Figure 1(c)) show that the case of January 25 is a perfect mature single-cell convection cumulonimbus with a mushroom-shaped structure. According to the typical features of a mature single-cell cumulonimbus, the whole structure of the cloud system can be separated into three regions: the cloud anvil region from 2217:48 to 2219:36 UTC, the convective core region from 2219:42 to 2222:30 UTC, and another small cloud anvil from 2222:36 to 2223:00 UTC. In the convective core, reflectivities around 50 dBZ are observed and the reflectivities above the altitude of 10 km are generally around 20 dBZ. The high reflectivities above 10 km observed in the convective tower region around 2221:00 UTC are even over 35 dBZ. The cloud top generally reaches to an altitude of 15 km excluding the small anvil region from 2222:36 to 2223:00 UTC. The highest cloud top approaching 17 km aligns with the convective tower.

Figure 1(a) indicates that in the cloud anvil region the high frequencies ($\geq$ 150 GHz) have larger brightness temperature depressions, the highest depression being observed at 220 GHz, then in sequence, those at the three water vapor channels and 150 GHz, and finally those at 89 GHz. However, when approaching the convective core region, the brightness temperature differences become smaller and smaller along with their largest

brightness temperature depressions. This observation is consistent with earlier studies of *Wang et al.* [1997]. It is due to the particle sizes of the frozen hydrometeors which are smaller in the cloud anvil than those in the convective core [e.g. *Heymsfield et al.*, 1996; *Wang et al.*, 1997, 1998]. Furthermore, the sensitivity of scattering to smaller frozen hydrometeors increases with frequency. The brightness temperature differences ΔT_{17}, ΔT_{13}, and ΔT_{37} have different characteristics in the entire deep convective cloud system (Figure 1(b)). At the edges of the deep convective cloud system (from 2217:30 to 2217:48 UTC and from 2223:00 to 2223:22 UTC), we have $\Delta T_{17} < \Delta T_{13} < \Delta T_{37} < 0$ K. This is due to the different temperature weighting functions of the three water vapor channels [*Burns et al.*, 1997; *Staelin and Chen*, 2000]. The channels further away from the center at 183.3 GHz can see deeper into the atmosphere where they detect higher temperatures in the clear sky. In nearly the complete deep convective cloud region from 2218:24 to 2222:36 UTC, we find the inverse relation $\Delta T_{17} \geq \Delta T_{13} \geq \Delta T_{37} > 0$ K, again because the channels further away from the center at 183.3 GHz can see deeper into the cloud, hence being subjected to greater scattering from the middle or low layers of the deep convective clouds [*Burns et al.*, 1997; *Wang et al.*, 1997]. In the two anvil regions, the values of ΔT_{17}, ΔT_{13}, and ΔT_{37} generally increase from the edges to the core. However, within the convective core region, when approaching the convective cell, the values of ΔT_{17}, ΔT_{13}, and ΔT_{37} decrease, but the relation $\Delta T_{17} \geq \Delta T_{13} \geq \Delta T_{37} > 0$ K still holds. This is because the temperature weighting functions of the three water vapor channels tend to be similar where there are large frozen hydrometeor contents [*Burns et al.*, 1997]. From the above analysis we conclude that the region with $\Delta T_{17} \geq \Delta T_{13} \geq \Delta T_{37} > 0$ K matches the entire region of the deep convective cloud system. Moreover, this deep convective cloud

system penetrates the TTL (14-18 km), This process is called convective overshooting [*Alcala and Dessler*, 2002].

Figure 2 shows the collocated observed data from the same instruments as in Figure 1 along the flight track of 1813:24 to 1816:14 UTC on 10 February. We identify three strong convective cells in this deep convective cloud system from the EDOP radar reflectivities (Figure 2(c)), with reflectivities over 40 dBZ. They are still as high as 20 dBZ in most regions above 10 km of the deep convective cloud system. The structure of the left deep convective cell is tilted towards the right. Similar to the case of 25 January, the brightness temperatures at $89 - 220$ GHz (Figure 2(a)) have a general negative correlation with the intensity of the deep convective cloud system (Figure 2(c)), the regions of large brightness temperature depressions corresponding to the convective cells. ΔT_{17}, ΔT_{13}, and ΔT_{37} (Figure 2(b)) do not show the exact behavior of $\Delta T_{17} \geq \Delta T_{13} \geq \Delta T_{37} > 0$ K for the entire flight track. At the left edge of the cloud (from 1813:24 to 1813:42 UTC), the tops of the tilted structure cloud are below 10 km. Although the EDOP radar reaches large reflectivities around 20 dBZ at the cloud tops, the order of ΔT_{17}, ΔT_{13}, and ΔT_{37} is the same as that for clear sky observed in the case of 25 January, namely $\Delta T_{17} < \Delta T_{13} < \Delta T_{37} < 0$ K. This behavior appears again in the region from 1815:21 to 1815:45 UTC where there are two cloud layers, the anvil cirrus at the altitude of $8 - 14$ km and the convective core below 8 km. The anvil cirrus has a high cloud top near the bottom of the TTL at 14 km, but with weak intensity (the EDOP reflectivities below 10 dBZ). The convective core is strong with EDOP reflectivities around 25 dBZ at the top, but this top is below 8 km. This feature again makes evident that the main contributions to the

radiances at the three water vapor channels are from the upper layers in deep convective clouds.

In the deep convective regions excluding the left edge of the cloud system from 1813:24 to 1813:51 UTC and the region from 1815:06 to 1815:45 UTC, the EDOP radar reflectivities are large (around 20 dBZ) above 10 km and the cloud tops exceed 14 km. We also can name these regions as convective overshooting regions because the cloud tops penetrate into the TTL. In these regions all values of ΔT_{17}, ΔT_{13}, and ΔT_{37} are positive (Figure 2(b)). Similar to the case of January 25, again the relation $\Delta T_{17} \geq \Delta T_{13} \geq \Delta T_{37} > 0$ K holds in convective overshooting regions. However, in the two small regions located around 1813:48, and 1815:06−1815:21 UTC the above mentioned relation does not hold. We use this fact to distinguish convective overshooting from deep convective clouds, i.e., the values of ΔT_{17}, ΔT_{13}, and ΔT_{37} remain positive but the order relation $\Delta T_{17} \geq \Delta T_{13} \geq \Delta T_{37} > 0$ K is not more valid. Concluding, from our analyses of the observations over the two deep convective cloud systems, we define two criteria:

$$\text{Deep convective cloud:} \qquad \Delta T_{17} \geq 0, \Delta T_{13} \geq 0, \text{ and } \Delta T_{37} \geq 0\,\text{K}, \tag{1}$$

$$\text{Convective overshooting:} \qquad \Delta T_{17} \geq \Delta T_{13} \geq \Delta T_{37} > 0\,\text{K}. \tag{2}$$

3. Confirmation and Generalization of the Criteria by Simulations

3.1. Cloud Model Data and Radiative Transfer Model

The Goddard Cumulus Ensemble (GCE) model [*Tao and Simpson*, 1993] is a dynamical cloud model, which uses nearby composite aircraft and radiosonde sounding as initial environmental field to simulate an oceanic tropical squall line. The model domain is a $128 \times 128 \times 31$ grid with a horizontal resolution of 1.5 km and vertical resolution varying

from 0.2 to 1.0 km from bottom to top (at 20 km altitude). The GCE cloud model distinguishes five hydrometeor types: cloud liquid water, rain water, cloud ice, snow, and graupel. Profiles of temperature and water vapor are also obtained along with profiles of the five hydrometeors. The GCE data at the model time of 360 minutes in the mature squall line are used for the simulations. Since our study is focussed on deep convective clouds, only clouds with top height above 10 km are considered. We have classified these clouds into four types, cirrus cloud, deep convective cloud, deep convective cloud with overshooting, and other clouds mainly including stratiform clouds and weak convective clouds. The classification results are shown in Figure 3(a).

The discrimination of cirrus clouds is based on the method of *Mace et al.* [2001] and *Luo et al.* [2003]. According to their method, to qualify a cloud layer as cirrus, the temperature at cloud top must be less than $-35°$C and the temperature at the level of maximum total ice water content must be less than $-20°$C. This method ensures that ice microphysical processes are dominant in the generation region near the cloud top, but excludes deep convective cloud layers that are capped by ice-phase clouds [*Luo et al.*, 2003]. Deep convective clouds normally have a large frozen hydrometeor water content in the upper layers [e.g. *Cifelli et al.*, 2002; *Skofronick-Jackson et al.*, 2003]. From the EDOP radar observations (Figures 1(c) and 2(c)), the radar reflectivities of the deep convective clouds at the altitude of 10 km are around 20 dBZ. This is in agreement well with the radar observations of two other mesoscale convective systems in the TRMM LBA [*Cifelli et al.*, 2002], where it has been shown that radar reflectivity at 10 km can be 20 dBZ for convective towers. This value at or above 14.5 km was also used to identify a convective tower [e.g. *Geerts et al.*, 2000; *Kelley and Stout*, 2004]. Using the empirical

relationship of *Heymsfield and Palmer* [1986] between radar reflectivity and cloud ice water content, 20 dBZ radar reflectivity corresponds to about 0.52 $\mathrm{g\,m^{-3}}$ cloud ice water content. Therefore, the GCE cloud model data with cloud top height above 10 km and the layers above 10 km having total ice water content values above 0.5 $\mathrm{g\,m^{-3}}$ are classified as deep convective clouds. The deep convective clouds with cloud top height above 14 km penetrate into the TTL are considered as convective overshooting [*Alcala and Dessler*, 2002]. The remaining components are classified into other clouds.

In this study, a microwave radiative transfer model (RTM) [*Kummerow et al.*, 1996] is used to calculate the microwave upwelling brightness temperatures between 89 and 183 GHz. The RTM considers the same five hydrometeor types as those obtained from the GCE cloud model data. All hydrometeors are treated as Mie spheres. The size distributions of rain, snow, and graupel are assumed to be exponentially distributed with

$$N(D) = N_0 \exp(-\lambda D), \tag{3}$$

where D is the diameter of particles, N_0 is the intercept parameter, and λ is the slope of the distribution depending on N_0, the density of hydrometeor, and the hydrometeor water content. N_0 values used in this study are 2.2×10^7 $\mathrm{m^{-4}}$ for rain, 10^8 $\mathrm{m^{-4}}$ for snow, and 4×10^6 $\mathrm{m^{-4}}$ for graupel. The same N_0 values have been used in the TRMM version 6 of 2A12 algorithm by Kummerow (Haiyan Jiang, personal communication). The densities of rain, snow, and graupel are 1.0 $\mathrm{g\,m^{-3}}$, 0.1 $\mathrm{g\,m^{-3}}$, and 0.6 $\mathrm{g\,m^{-3}}$, respectively. *Wang et al.* [1997, 1998] suggested that cloud ice in the upper portion of convection should be taken into account at high frequencies of the AMSU-B channels. The distribution of cloud ice included in this version of the RTM is the one given by the fit to observed cloud ice distributions by *Heymsfield and Platt* [1984]. The particle size of cloud water is gamma

distributed according to *Liou* [1992]. The densities of cloud ice and cloud liquid water are respectively 0.917 $\mathrm{g\,m^{-3}}$ and 1.0 $\mathrm{g\,m^{-3}}$.

3.2. Identification of Deep Convective Clouds from Simulated Brightness Temperatures

The profiles of hydrometeors, temperature, and water vapor are given as input for the RTM to simulate brightness temperatures at 183.3 ± 1, 183.3 ± 3, and 183.3 ± 7 GHz. For precipitating clouds, the three water vapor channels are independent of the surface emissivity [*Staelin and Chen*, 2000; *Bennartz and Bauer*, 2003], so the surface emissivities at these frequencies are set to a typical value of 0.7 to represent oceans [*Muller et al.*, 1994]. In order to conform with the MIR measurements and AMSU-B observations, the effects of double side bands in the water vapor channels are taken into account by averaging the simulated brightness temperatures at the upper and lower sideband [*Wang et al.*, 1997], such as averaging the simulated brightness temperatures at $183.3 - 1$ and 183.3+1 GHz for the simulated brightness temperature at 183.3 ± 1 GHz, etc. Because our criteria are derived from the MIR measurements at nadir, only nadir simulated brightness temperatures are used in this section. Then, we apply criterion (1) for deep convective clouds and criterion (2) for convective overshooting (Figure 3(b)). The locations and ranges of deep convective clouds and overshooting determined by criteria (1) and (2) match well with those directly determined from the GCE cloud model data. Only two very small deep convective clouds located at (x=42, y=75) and (x=52, y=75) are estimated by our criteria that are not shown in the GCE cloud model data. Overall, that our criteria work satisfactorily.

3.3. Criteria for Different Viewing Angles

Until now, our analyses are only focused on nadir observations and simulations. However, AMSU-B working in cross-track mode looks at the atmosphere with a wide variation of viewing angles. The centers of scanning beam of AMSU-B vary in the range of $0.62^\circ - 58.73^\circ$ at a nominal satellite altitude of 850 km. Such variation of the viewing angle results in slant paths influencing the measurements. We modify criteria (1) and (2) by introducing threshold temperatures T_D for the deep convective cloud criterion and T_O for the convective overshooting criterion:

$$\text{Deep convective cloud:} \qquad \Delta T_{17} \geq T_D, \Delta T_{13} \geq T_D, \text{ and } \Delta T_{37} \geq T_D, \tag{4}$$

$$\text{Convective overshooting:} \qquad \Delta T_{17} \geq \Delta T_{13} \geq \Delta T_{37} > T_O. \tag{5}$$

In order to adjust the threshold T_D for deep convective clouds to different viewing angles, we define for each viewing angle θ an empirical quality measure,

$$C(\theta, T_D) = \frac{A_O(\theta, T_D)}{A(0,0) + A(\theta, T_D) - A_O(\theta, T_D)}, \tag{6}$$

where $A(\theta, T_D)$ is the total area of deep convective clouds in the GCE model field determined from the simulated brightness temperatures according to criterion (4) at viewing angle θ and threshold T_D, $A(0,0)$ is the same, but at viewing angle $\theta = 0^\circ$ and with $T_D = 0$ K, which is identical to criterion (1), $A_O(\theta, T_D)$ is the overlap region of $A(\theta, T_D)$ and $A(0,0)$. $C(\theta, T_D)$ varies between 0 to 1. For each $\theta = 0^\circ, 5^\circ, ..., 60^\circ$ we select the threshold T_D maximizing $C(\theta, T_D)$, i.e. making $A(\theta, T_D)$ most similar to $A(0,0)$ obtained at nadir which is considered as the true value. The maximum values of $C(\theta, T_D)$ are clearly pronounced (Figure 4). The maximum values of $C(\theta, T_D)$ are almost equal to 1 at viewing angles below 35°, still higher than 0.9 at viewing angles between 40° and 50°,

and even over 0.7 at viewing angles of 55° and 60°. This indicates the high coincidence of criteria (4) for different viewing angles and (1) for nadir observations. A second degree polynomial fit for threshold value T_D and all considered viewing angles θ (unit in degree) yield

$$T_D = 0.04761 - 0.01678\,\theta + 0.00599\,\theta^2 \tag{7}$$

with a standard deviation of 0.18 K.

For convective overshooting, the empirical quality measure $C(\theta, T_O)$ which has the similar definition as $C(\theta, T_D)$ is also investigated (Figure 4). At all viewing angles, $C(\theta, T_O)$ is generally stable when T_O is below 15 K. $C(\theta, T_O)$ quickly decreases when T_O is above 15 K. At viewing angles below 30°, the maximum values of $C(\theta, T_O)$ are between 0.95 and 0.8. But at viewing angles above 35°, the highest $C(\theta, T_O)$ values are below 0.6, even lower than 0.2 at the viewing angle 60°. Thus, $T_O = 0$ K is used as the threshold value for criterion (5) to detect convective overshooting. But unlike criterion (4) for deep convective clouds, criterion (5) for convective overshooting works well only at satellite viewing angles below 30°.

4. Application to AMSU-B Data

4.1. Identification of Cold Clouds Associated with Precipitation

Initially, we use a method adapted from *Greenwald and Christoper* [2002] to identify the cold clouds associated with precipitation. *Greenwald and Christoper* [2002] found that the background brightness temperature at 183.3 ± 1 GHz is remarkably stable from region to region with an overall mean and standard deviation of 241.9 ± 2.1 K, and cold clouds associated with precipitation have an average brightness temperature depression of about

7 K. So if the overall mean value of background brightness temperature at 183.3 ± 1 GHz is set as 242 K, the brightness temperature at 183.3 ± 1 GHz below 235 K ($= 242 - 7$ K) can be used as the criterion for identifying the cold clouds associated with precipitation. The threshold value of 235 K is also used by *Staelin and Chen* [2000] for the brightness temperature at 183.3 ± 1 GHz in saturated atmospheres. They documented that hydrometeors in precipitating clouds lower the brightness temperatures at 183.3 ± 1 GHz below those observed over saturated atmospheres (i.e., 235 K). Hence, if the brightness temperature at 183.3 ± 1 GHz is below 235 K, we consider that the field of view of AMSU-B contains the cold clouds associated with precipitation. Once we have identified the cold clouds associated with precipitation, we detect deep convective clouds and convective overshooting by our criteria (4) and (5). Our criteria are applied to data of AMSU-B onboard NOAA-16 collected in the four three-month seasons from March 2002 to February 2003, i.e., March to May 2002 (MAM), June to August 2002 (JJA), September to November 2002 (SON), and December 2002 to February 2003 (DJF). Deep convective clouds and convective overshooting are averaged over $5^\circ \times 5^\circ$ longitude-latitude grid boxes in the topics (30°N-30°S) and over the indicated season.

4.2. Distributions of Deep Convective Clouds

The distributions of mean deep convective cloud fractions for the four seasons are shown in Figure 5. The monthly $1^\circ \times 1^\circ$ TRMM 3B43 rainfall product [*Huffman et al.*, 1997] estimated from TRMM, geosynchronous IR, and rain gauge data are averaged over the same three-month seasons. Rainfall exceeding 3 mm day^{-1} is enclosed by red contour lines. In agreement with the results of *Alcala and Dessler* [2002], the geographical distributions of deep convective clouds show a good correspondence with the TRMM 3B43 rainfall con-

tour, qualitatively confirming our detection of deep convective clouds. The distributions of deep convective clouds and TRMM 3B43 rainfall have similar characteristics as those of the time-mean convection described by *Hendon and Woodberry* [1993]. These include the pronounced ITCZ across the Pacific and the Atlantic Oceans, the pronounced South Pacific Convergence Zone (SPCZ), intense centers of convection over tropical Africa and tropical America, and the center of convection over the Indian Ocean.

The most prominent feature of the distributions of the deep convective clouds is the seasonal variability (Figure 5). In MAM and DJF, the distributions of deep convective clouds are dominantly in the Southern Hemisphere (SH). In contrast, they are shifted to the Northern Hemisphere (NH) in JJA and SON. In general, the summer hemisphere has more convective activity than the winter hemisphere, such as the NH in JJA and the SH in DJF. The deep convective clouds migrate from the NH in JJA and SON to the SH in DJF and MAM. Similar seasonal shifting was also noted by *Chen et al.* [e.g. 1996], *Gettelman et al.* [2002], *Alcala and Dessler* [2002], and *Jiang et al.* [2004]. *Chen et al.* [1996] studied the multiscale variability of deep convection in relation to large-scale circulation in the warm-pool region during Tropical Ocean Global Atmosphere Coupled Ocean-Atmosphere Response Experiment (TOGA COARE). They documented that the dominant convective variability was associated with the seasonal cycle with a southward shift from the NH in October-November to the SH in January-February. The deep convective clouds in the pronounced narrow ITCZ have their local maximum fractions between 0° and 10° latitude [*Chen et al.*, 1996]. In general, deep convective clouds seem to appear more frequently over oceans in the ITCZ and SPCZ (excluding in MAM). The SPCZ is more apparent

in MAM and DJF than other two seasons, in agreement with the findings of *Chen et al.* [1996].

Comparing with some other analyses using infrared measurements [*Chen et al.*, 1996; *Mapes and Houze*, 1993; *Machado et al.*, 2002], our deep convective cloud fractions are smaller, the averaged deep convective cloud fraction is about 0.3% in the entire topics and about 1.0% in the ITCZ and SPCZ for the four seasons. Using -38°C (cloud top height about 10 km) as the infrared temperature threshold, *Chen et al.* [1996] found that deep convective cloud fractions in the ITCZ and SPCZ are about $10-20\%$. The same infrared temperature threshold was also used by *Mapes and Houze* [1993], but for moderately cold cloud. *Machado et al.* [2002] used the same threshold for high clouds, and found that the diurnal variation of the high cloud fraction varies between 3% and 29% in the TRMM Wet Season Atmospheric Mesoscale Campaign/LBA (TRMM-WETAMC/LBA) region ($63.3^\circ - 61.0^\circ$W, $12.1^\circ - 9.8^\circ$S) in January-February 1999. It seems that the high fractions are due to the high infrared temperature thresholds. The clouds with cloud top temperatures below -40°C include thin high-top nonprecipitating cloud, deep high-top precipitating cloud, anvil with stratiform precipitating cloud, and deep convective precipitating cloud [*Liu et al.*, 1995]. The deep convective cloud fraction derived with the cold infrared temperature threshold at -58°C by *Gettelman et al.* [2002] has a similar range as that from *Chen et al.* [1996]. An even colder infrared temperature threshold of -65°C (cloud top height about 15 km) was also used to identify tropical deep convective clouds [e.g. *Mapes and Houze*, 1993; *Chen et al.*, 1996; *Hall and Haar*, 1999; *Machado et al.*, 2002; *Gettelman et al.*, 2002]. In general, cloud tops colder than -65°C cover about 20% of the area with cloud tops colder than -38°C [*Mapes and Houze*, 1993]. With the

−65°C infrared temperature threshold, *Chen et al.* [1996] found that the deep convective cloud fraction is below 6% in the ITCZ and SPCT. The same result was reported by *Machado et al.* [2002] in the TRMM-WETAMC/LBA. With a −63°C infrared temperature threshold they obtained diurnal variations of the deep convective cloud fraction ranging from 0 to 6%. With this threshold, *Gettelman et al.* [2002] found a deep convective fraction of 5% in October 1991 in the region from 64° − 77°E and 4° − 7°N. With respect to the deep convective fractions derived by high infrared temperature thresholds (i.e., −38°C), our derived deep convective fractions approach those derived by low infrared temperature threshold (i.e., −65°C). *Hall and Haar* [1999] found that the deep convective clouds only covered about 2% of the total possible area in the west pacific for JJA and November to January. Our derived deep convective fractions in the west Pacific in JJA and DJF are generally close to this result (Figure 5).

There are two possible sources of uncertainty for the deep convective cloud fractions derived from the low infrared temperature threshold (i.e., −65°C). One is an overestimation because high cirrus clouds are tightly connected with deep convective clouds fractions [*Chou and Neelin*, 1999]. Also the −65°C cloud top temperature corresponds to the beginning level of convective overshooting (14 km) [*Hall and Haar*, 1999; *Kelley and Stout*, 2004]. Therefore, with this threshold, only convective overshooting can be detected whereas the deep convective clouds with top height below 14 km (cloud top temperature warmer than −65°C) can not be detected. This is the second uncertainty that results in an underestimation of deep convective clouds. *Liu et al.* [1995] identified deep convective precipitating clouds in the western equatorial Pacific Ocean warm pool region (15°S − 15°N, 130°E − 180°E) for the period from November 1992 to February 1993. A

−40°C infrared temperature threshold was used to discriminate the high clouds with top height above 10 km. A microwave index derived from SSM/I brightness temperatures at 19 and 89 GHz was used to detect microwave scattering and emission from precipitating clouds. This approach considered both the cloud top and information on precipitation of deep convective clouds. Their results overcame the two uncertainties of the method for identifying deep convective clouds only by the choice of a low infrared temperature threshold. Their results showed that deep convective precipitating clouds account for 1.05% of the total cloudy pixels. In this region, the average total cloud fraction is about 76% [*Hartmann et al.*, 2001], so the deep convective cloud fraction in the region is about 0.8% (=1.05% × 76%) from the results of *Liu et al.* [1995]. Our averaged deep convective fraction in this region is about 0.75%, which is quite similar to the result of *Liu et al.* [1995].

4.3. Distributions of Convective Overshooting

The distributions of convective overshooting, i.e., those deep convective clouds that penetrate into the TTL, grouped by same seasons as those for deep convective clouds, are shown in Figure 6. The contour lines enclosing all sea surface temperatures (SST) greater than 28°C derived from the monthly mean reconstructed SST data of NOAA Climate Diagnostics Center (CDC) are also shown. Because the criterion for detecting convective overshooting are only valid for viewing angles from 0° to 30°, only such observations have been used. In order to display the deep convective cloud fractions that give rise to overshooting, and the convective overshooting fractions, the convective overshooting fraction of deep convective clouds is weighted by the convective overshooting fraction of total number of samples. It is named weighted convective overshooting fraction.

The spatial pattern and seasonal variability of the distributions of the weighted convective overshooting fraction are very similar as those of the deep convective clouds. The apparent different feature of the distributions of convective overshooting is that the higher fractions obviously appear over land, not over ocean. This indicates that, although deep convective clouds generally have high fractions over ocean (Figure 5), those that penetrate into the TTL are more frequent over land (Figure 6). This feature is in agreement with the results of the TRMM PR [*Nesbitt et al.*, 2000; *Toracinta et al.*, 2002; *Alcala and Dessler*, 2002], and observations obtained from aircraft radar [*Heymsfield et al.*, 1996].

Analyzing TRMM observations in two tropical continental (tropical Africa and South America) and tropical oceanic regions (the east Pacific and west Pacific) in August-September-October 1998 (ASO 1998), *Nesbitt et al.* [2000] and *Toracinta et al.* [2002] reported that tropical continental convective clouds often have larger magnitudes of PR reflectivity and smaller decrease in reflectivity with height than tropical oceanic convective clouds. Especially, *Nesbitt et al.* [2000] found that deep convective clouds seem to favor the western side of the South America and away from the Atlantic coast in ASO 1998. This feature is also apparent in our results in SON and JJA. On the other hand, the similar feature is also observed in South Africa in MAM and SON. Thus, these features are caused by other reasons besides the focusing mechanism for mesoscale cloud systems, which is due to the foothills of Andes Mountains indicated by *Nesbitt et al.* [2000]. They also pointed out that convection over Africa has the strongest and east Pacific has the weakest PR reflectivities. Using TRMM data in the west Pacific and east Pacific, similar regions as those used by *Nesbitt et al.* [2000], *Berg et al.* [2002] also found that the east Pacific has shallower clouds than the west Pacific from December 1999 to February

2000. Our results confirm these findings (Figure 6, DJF). However, from our results, we can state even more detailed that deep convective clouds over South America or Central America have the highest frequency to penetrate into the TTL in most seasons. The region with the most frequent oceanic convective overshooting changes with seasons, such as the SPCT in MAM and the ITCZ over the east Pacific in JJA.

The geographical distributions of the oceanic convective overshooting fractions show a general correspondence with the 28°C SST contour line in Figure 6. This is in agreement with the mechanism stated by *Roca et al.* [2002] that the convective clouds grow deeper and reach colder temperatures as the surface warms. However, in the ITCZ over the east Pacific and the Atlantic, it seems that the distributions of convective overshooting are generally broader than the regions contained within the 28°C SST conour line. In other regions over ocean, we found the opposite. This feature can probably be explained by the relationships between deep convection, SST, and surface wind convergence [*Fu et al.*, 1990]. They suggested that deep convective cloud is enhanced in regions where either the SST is greater than 28°C in the absence of strong surface wind divergence, or the SST is less than 28°C, combined with strong surface wind convergence.

The averaged amount of convective overshooting is about 22% of total deep convective cloud. This ratio is in agreement with the ratio of cloud tops colder than −65°C to the area with cloud tops colder than −38°C (about 20%) [*Mapes and Houze*, 1993]. On the other hand, our result is much larger than that the value of about 5% found by *Alcala and Dessler* [2002]. They also noted that the amount is influenced by the sensitivity of the TRMM PR and increasing the reflectivity threshold from 12 to 17 dBZ would increase the amount by about a factor of two. *Alcala and Dessler* [2002] documented that their results

can be considered as a lower limit. Based on this, it seems that our result as depicted in Figure 6 is close to real occurrence.

5. Conclusion

The AMSU-B water vapor channels have unique advantages, such as high sensitivity to frozen hydrometeors in precipitating clouds [e.g. *Burns et al.*, 1997; *Wang et al.*, 1997; *Bennartz and Bauer*, 2003], different sensitivities to vertical distributions of frozen hydrometeors [e.g. *Burns et al.*, 1997; *Bennartz and Bauer*, 2003], and negligible impact of the ground surface and liquid water cloud in the lower to middle troposphere [e.g. *Muller et al.*, 1994; *Wang et al.*, 1997; *Greenwald and Christoper*, 2002; *Bennartz and Bauer*, 2003]. We have derived methods to detect deep convective clouds and convective overshooting using the brightness temperature differences between the three water vapor channels centered at 183.3 GHz from aircraft observations and model simulations. The criterion for tropical deep convective clouds is $\Delta T_{17} \geq T_D$, $\Delta T_{13} \geq T_D$, and $\Delta T_{37} \geq T_D$. Model simulations determined T_D, which increases with the viewing angle across the swath of AMSU-B. The criterion for convective overshooting is $\Delta T_{17} \geq \Delta T_{13} \geq \Delta T_{37} > 0$ K, but only for AMSU-B viewing angles below 30°.

The methods are applied to AMSU-B data to obtain the distributions of deep convective clouds and convective overshooting in the tropics (30°S to 30°N) for four three-month seasons from March 2002 to February 2003. The good correspondence of the geographical distributions of deep convective clouds with high precipitation (Figure 5) confirms the methods. The main regions of deep convective clouds and convective overshooting are over the ITCZ, the SPCZ, tropical Africa, tropical America, and the Indian Ocean. The distributions vary with the season. Deep convective clouds and convective overshooting

migrating from the winter hemisphere to the summer hemisphere. The seasonal shifting is in agreement with the results of *Chen et al.* [1996], *Gettelman et al.* [2002], *Alcala and Dessler* [2002], and *Jiang et al.* [2004]. Although deep convective clouds frequently appear over oceans in the ITCZ and SPCZ, deep convective clouds penetrating into the TTL are more frequent over land. This result is consistent with those of *Nesbitt et al.* [2000], *Toracinta et al.* [2002], and *Alcala and Dessler* [2002]. It is also found that, deep convective clouds seem to favor the western side of the continents of South America and tropical Africa in some seasons. The matching and dismatching of the weighted convective overshooting fractions and the 28°C SST contour lines indicate that the enhancing mechanism of deep convective clouds is not only due to the warmer SST, but is also related to such factors as surface wind convergence [*Fu et al.*, 1990].

The averaged amount of the deep convective cloud fractions in the entire tropics is about 0.3% and 22% of them can penetrate into the TTL as convective overshooting. Our deep convective cloud fractions are smaller than the results derived from infrared measurements. The difference between our deep convective cloud fractions and those derived from infrared measurements probably indicate that high cirrus clouds have large contributions on deep convective cloud fractions derived from infrared measurements [*Chou and Neelin*, 1999]. But when restricted to the western equatorial Pacific Ocean warm pool region, our averaged deep convective cloud fraction of about 0.75% is in well agreement with the result of *Liu et al.* [1995] of about 0.8%.

Although the amount of deep convective clouds penetrating into the TTL in the entire tropics is small (about 0.07%), it has important impact on the physical and chemical processes in the TTL and in the stratosphere [e.g. *Lelieveld and Crutzen*, 1994; *Holton*

et al., 1995; *Thompson et al.*, 1997; *Sherwood and Dessler*, 2001; *Dessler*, 2002; *Gettelman et al.*, 2002; *Andronache et al.*, 2002]. The AMSU-B and similar AMSU/HSB (Humidity Sounder for Brazil) sensors onboard the platforms NOAA-15, 16, 17, and Aqua promise a high potential contributing to an improved understanding of the important role of deep convective clouds in the tropics by future work in two directions: First, all of the mentioned platforms carry also IR sensors allowing to derive similar parameters of the same time and space. A synergy potential of both sensor types is to be expected, but unexplored. Second, as the mentioned platforms can observe each point on earth about eight times per day [*Chen and Staelin*, 2003], combining measurements of all these microwave and IR sensors provides a unique tool to observe the evolution of deep convective clouds in time and space. Both types of investigation will contribute to better understand the features of deep convective clouds and convective overshooting in the tropics, so as to assess the influence of deep coonvective clouds and convective overshooting on the physical and chemical processes in the TTL and stratosphere.

Acknowledgments. We thank J. Wang and G. Skofronick-Jackson for providing us with GCE cloud model data; C. Kummerow for providing and helping us with his RTM codes; H. Jiang for helping with the parameters of particle size distribution; P. Singh Chauhan for improving the original English text. We wish to thank J. Wang and P. Racette for production of the MIR data; G. Heymsfield and N. Ferreira for the production of the EDOP data; L. Neclos from the Comprehensive Large Array-data Stewardship System (CLASS) of the NOAA for providing the AMSU-B data. We also thank the Distributed Active Archive Center (DAAC) at the Goddard Space Flight Center, which archives and distributes the MIR and EDOP data under sponsorship of NASA's Earth Sci-

ence Enterprise. The rainfall data used in this study were acquired as part of the TRMM. The sea surface temperature data are provided by the NOAA-CIRES Climate Diagnostics Center. G. Hong is grateful to the Gottlieb Daimler- und Karl Benz- Foundation and University of Bremen for this support.

References

Alcala, C. M., and A. E. Dessler (2002), Observations of deep convection in the tropics using the Tropical Rainfall Measuring Mission (TRMM) precipitation radar, *J. Geophys. Res.*, *107*(D24), 4792, doi:10.1029/2002JD002457.

Anagnostou, E. N., and C. Kummerow (1997), Stratiform and convective classification of rainfall using SSM/I 85-GHz brightness temperature observations, *J. Atmos. Ocean. Technol.*, *14*, 570–575.

Andronache, C., L. J. Donner, C. J. Seman, and R. S. Hemler (2002), A study of the impact of the Intertropical Convergence Zone on aerosols during INDOEX, *J. Geophys. Res.*, *107*(D19), 8027, doi:10.1029/2001JD900248.

Bennartz, R., and P. Bauer (2003), Sensitivity of microwave radiances at 85-183 GHz to precipitating ice particles, *Radio Sci.*, *38*(4), 8075, doi:10.1029/2002RS002626.

Bennartz, R., A. Thoss, A. Dybbroe, and D. B. Michelson (2002), Precipitation analysis using the Advanced Microwave Sounding Unit in support of nowcasting applications, *Meteorol. Appl.*, *9*, 177–189.

Berg, W., C. Kummerow, and C. A. Morales (2002), Differences between east and west Pacific rainfall systems, *J. Climate*, *15*, 3659–3672.

Burns, B. A., X. Wu, and G. R. Diak (1997), Effects of precipitation and cloud ice on brightness temperatures in AMSU moisture channels, *IEEE Trans. Geosci. Remote Sens.*, *35*, 1429–1437.

Cecil, D. J., E. J. Zipser, and S. W. Nesbitt (2002), Reflectivity, ice scattering, and lightning characteristics of hurricane eyewalls and rainbands. Part I: Quantitative description, *Mon. Weather Rev.*, *130*, 769–784.

Chen, F. W., and D. H. Staelin (2003), AIRS/AMSU/HSB precipitation estimates, *IEEE Trans. Geosci. Remote Sens.*, *41*, 410–417.

Chen, F. W., and D. H. Staelin (2004), Global precipitation climatology from AMSU passive microwave satellite observations, paper presented at 84th American Meteorological Society (AMS) Annual Meeting, Amer. Meteor. Soc., Seattle, WA.

Chen, S. S., R. A. H. Jr., and B. E. Mapes (1996), Multiscale variability of deep convection in relationship to large-scale circulation in TOGA COARE, *J. Atmos. Sci.*, *53*, 1380–1409.

Chou, C., and J. D. Neelin (1999), Cirrus detrainment-temperature feedback, *Geophys. Res. Lett.*, *26*, 1295–1298.

Cifelli, R., W. A. Petersen, L. D. Carey, S. A. Rutledge, and M. A. F. da Silva Dias (2002), Radar observations of the kinematic, microphysical, and precipitation characteristics of two MCSs in TRMM LBA, *J. Geophys. Res.*, *107*(D20), 8077, doi: 10.1029/2000JD000264.

DeMott, C. A., and S. A. Rutledge (1998), The vertical structure of TOGA COARE convection. Part I: Radar echo distributions, *J. Atmos. Sci.*, *55*, 2730–2747.

Dessler, A. E. (2002), The effect of deep, tropical convection on the tropical tropopause layer, *J. Geophys. Res.*, *107*(D3), 4033, doi:10.1029/2001JD000511.

Di Giuseppe, F., and A. M. Tompkins (2003), Three-dimensional radiative transfer in tropical deep convective clouds, *J. Geophys. Res.*, *108*(D23), 4741, doi: 10.1029/2003JD003392.

Eyre, J. R. (1990), The information content of data from operational satellite sounding systems: A simulation study, *Q. J. R. Meteorol. Soc.*, *116*, 401–434.

Fu, R., A. D. D. Genio, and W. B. Rossow (1990), Behavior of deep convective clouds in the tropical Pacific deduced from ISCCP radiances, *J. Climate*, *3*, 1129–1152.

Geerts, B., G. M. Heymsfield, L. Tian, J. B. Halverson, A. Guillory, and M. I. Mejia (2000), Hurricane Georges's landfall in the Dominican Republic: Detailed airborne Doppler radar imagery, *Bull. Amer. Meteorol. Soc.*, *81*, 999–1018.

Gettelman, A., M. L. Salby, and F. Sassi (2002), The distribution and influence of convection in the tropical tropopause region, *J. Geophys. Res.*, *107*(D10), 4080, doi: 10.1029/2001JD001048.

Greenwald, T. J., and S. A. Christoper (2002), Effect of cold clouds on satellite measurements near 183 GHz, *J. Geophys. Res.*, *107*(D13), 4170, doi:10.1029/2000JD000258.

Gu, G., and C. Zhang (2002), Cloud components of the Intertropical Convergence Zone, *J. Geophys. Res.*, *107*(D21), 4565, doi:10.1029/2002JD002089.

Hall, T. J., and T. H. V. Haar (1999), The diurnal cycle of west Pacific deep convection and its relation to the spatial and temporal variations of tropical MCSs, *J. Atmos. Sci.*, *56*, 3401–3415.

Hartmann, D. L., L. A. Moy, and Q. Fu (2001), Tropical convection and the energy balance at the top of the atmosphere, *J. Climate*, *14*, 4495–4511.

Hendon, H. H., and K. Woodberry (1993), The diurnal cycle of tropical convection, *J. Geophys. Res.*, *98*(D9), 16,623–16,637.

Heymsfield, A. J., and A. G. Palmer (1986), Relationships for deriving thunderstorm anvil ice mass for CCOPE storm water budget estimates, *J. Clim. Appl. Meteor*, *25*, 691–702.

Heymsfield, A. J., and C. M. R. Platt (1984), A parameterization of the particle size spectrum of ice clouds in terms of the ambient temperature and the ice water content,

J. Atmos. Sci., *41*, 846–855.

Heymsfield, G. M., and R. Fulton (1988), Comparison of high-altitude remote aircraft measurements with the radar structure of an Oklahoma thunderstorm: Implications for precipitation estimation from space, *Mon. Weather Rev.*, *116*, 1157–1174.

Heymsfield, G. M., J. M. Shepherd, S. W. Bidwell, W. C. Boncyk, I. J. Caylor, S. Ameen, and W. S. Olson (1996), Structure of Florida thunderstorms using high-altitude aircraft radiometer and radar observations, *J. Appl. Meteorol.*, *35*, 1736–1762.

Heymsfield, G. M., B. Geerts, and L. Tian (2000), TRMM Precipitation Radar reflectivity profiles as compared with high-resolution airborne and ground-based radar measurements, *J. Appl. Meteorol.*, *39*, 2080–2102.

Highwood, E. J., and B. J. Hoskins (1998), The tropical tropopause, *Q. J. R. Meteorol. Soc.*, *124*, 1579–1604.

Holton, J. R., P. H. Haynes, A. R. Douglass, R. B. Rood, and L. Pfister (1995), Stratosphere-troposphere exchange, *Rev. Geophys.*, *33*, 403–439.

Hong, Y., C. Kummerow, and W. S. Olson (1999), Separation of convective and stratiform precipitation using microwave brightness temperature, *J. Appl. Meteorol.*, *38*, 1195–1213.

Huffman, G. J., R. F. Adler, P. Arkin, A. Chang, R. Ferraro, A. Gruber, J. Janowiak, A. McNab, B. Rudolf, and U. Schneider (1997), The global precipitation climatology project (GPCP) combined precipitation dataset, *Bull. Amer. Meteor. Soc.*, *78*, 5–20.

Jiang, J. H., B. Wang, K. Goya, K. Hocke, S. D. Eckermann, J. Ma, D. L. Wu, and W. J. Read (2004), Geographical distribution and interseasonal variability of tropical deep convection: UARS MLS observations and analyses, *J. Geophys. Res.*, *109*(D03111),

doi:10.1029/2003JD003756.

Kelley, O., and J. Stout (2004), Convective towers in eyewalls of tropical cyclones observed by the TRMM Precipitation Radar in 1998-2001, paper presented at 20th Conference on Weather Analysis and Forecasting, Amer. Meteor. Soc., Seattle, WA.

Kidder, S. Q., M. D. Goldberg, R. M. Zehr, M. DeMaria, J. F. W. Purdom, C. S. Velden, N. C. Grody, and S. J. Kusselson (2000), Satellite analysis of tropical cyclones using the Advanced Microwave Sounding Unit (AMSU), *Bull. Amer. Meteorol. Soc.*, *81*, 1241–1260.

Kummerow, C., W. S. Olson, and L. Giglio (1996), A simplified scheme for obtaining precipitation and vertical hydrometeor profiles from passive microwave sensors, *IEEE Trans. Geosci. Remote Sens.*, *34*, 1213–1232.

Lelieveld, J., and P. J. Crutzen (1994), Role of deep convection in the ozone budget of the troposphere, *Science*, *264*, 1759–1761.

Liou, K. N. (1992), *Radiation and cloud processes in atmosphere: Theory, Observation, and Modeling*, 487 pp., Oxford Univ. Press, Oxford.

Liu, G., J. A. Curry, and R.-S. Sheu (1995), Classification of clouds over the western equatorial Pacific Ocean using combined infrared and microwave satellite data,, *J. Geophys. Res.*, *100*, 13,811–13,826.

Luo, Y., S. K. Krueger, G. G. Mace, and K.-M. Xu (2003), Cirrus cloud properties from a cloud-resolving model simulation compared to cloud radar observations, *J. Atmos. Sci.*, *60*, 510–525.

Mace, G. G., E. E. Clothiaux, and T. P. Ackerman (2001), The composite characteristics of cirrus clouds: Bulk properties revealed by one year of continuous cloud radar data,

J. Climate, *14*, 2185–2203.

Machado, L. A. T., H. Laurent, and A. A. Lima (2002), Diurnal march of the convection observed during TRMM-WETAMC/LBA, *J. Geophys. Res.*, *107*(D20), 8064, doi:10.1029/2001JD000338.

Mapes, B. E., and R. A. Houze Jr. (1993), Cloud clusters and superclusters over the oceanic warm pool, *Mon. Wea. Rev.*, *121*, 1398–1415.

Muller, B. M., H. E. Fuelberg, and X. Xiang (1994), Simulations of the effects of water vapor, cloud liquid water, and ice on AMSU moisture channel brightness temperatures, *J. Appl. Meteorol.*, *33*, 1133–1154.

Nesbitt, S. W., E. J. Zipser, and D. J. Cecil (2000), A census of precipitation features in the tropics using TRMM: Radar, ice scattering, and lightning observations, *J. Climate*, *13*, 4087–4106.

Rickenbach, T. M., and S. A. Rutledge (1998), Convection in TOGA COARE: Horizontal scale, morphology and rainfall production, *J. Atmos. Sci.*, *55*, 2715–2729.

Roca, R., M. Viollier, L. Picon, and M. Desbois (2002), A multisatellite analysis of deep convection and its moist environment over the Indian Ocean during the winter monsoon, *J. Geophys. Res.*, *107*(D19), 8012, doi:10.1029/2000JD000040.

Sherwood, S. C., and A. E. Dessler (2000), On the control of stratospheric humidity, *Geophys. Res. Lett.*, *27*, 2513–2516.

Sherwood, S. C., and A. E. Dessler (2001), A model for transport across the tropical tropopause, *J. Atmos. Sci.*, *58*, 765–779.

Simpson, J., J. Halverson, H. Pierce, C. Morales, and T. Iguchi (1998), Eyeing the eye: Exciting early stage science results from TRMM, *Bull. Amer. Meteorol. Soc.*, *79*, 1711.

Skofronick-Jackson, G. M., A. J. Gasiewski, and J. R. Wang (2002), Influence of microphysical cloud parameterizations on microwave brightness temperatures, *IEEE Trans. Geosci. Remote Sens.*, *40*, 187–196.

Skofronick-Jackson, G. M., J. R. Wang, G. M. Heymsfield, R. Hood, W. Manning, R. Meneghini, and J. A. Weiman (2003), Combined radiometer-radar microphysical profile estimations with emphasis on high-frequency brightness temperature observations, *J. Appl. Meteorol.*, *42*, 476–487.

Staelin, D. H., and F. W. Chen (2000), Precipitation observations near 54 and 183 GHz using the NOAA-15 satellite, *IEEE Trans. Geosci. Remote Sens.*, *38*, 2322–2332.

Tao, W.-K., and J. Simpson (1993), Goddard cumulus ensemble model. Part I: Model description, *Terr. Atmos. Oceanic Sci.*, *4*, 35–72.

Thompson, A. M., W.-K. Tao, K. E. Pickering, J. R. Scala, and J. Simpson (1997), Tropical deep convection and ozone formation, *Bull. Amer. Meteorol. Soc.*, *78*, 1043–1054.

Thuburn, J., and G. C. Craig (2002), On the temperature structure of the tropical substratosphere, *J. Geophys. Res.*, *107*(D2), 4017, doi:10.1029/2001JD000448.

Toracinta, E. R., D. J. Cecil, E. J. Zipser, and S. W. Nesbitt (2002), Radar, passive microwave, and lightning characteristics of precipitating systems in the tropics, *Mon. Weather Rev.*, *130*, 802–824.

Wang, J. R., J. Zhan, and P. Racette (1997), Storm-associated microwave radiometric signatures in the frequency range of 90-220 GHz, *J. Atmos. Ocean Technol.*, *14*, 13–31.

Wang, J. R., J. Zhan, and P. Racette (1998), Multiple aircraft microwave observations of storms over the western Pacific Ocean, *Radio Sci.*, *33*, 351–368.

Weng, F., L. Zhao, R. R. Ferraro, G. Poe, X. Li, and N. C. Grody (2003), Advanced microwave sounding unit cloud and precipitation algorithms, *Radio Sci.*, *38*(4), 8068, doi:10.1029/2002RS002679.

Zhao, L., and F. Weng (2002), Retrieval of ice cloud parameters using the Advanced Microwave Sounding Unit, *J. Appl. Meteorol.*, *41*, 384–395.

Figure Captions

Figure 1. (a) The MIR brightness temperatures, (b) brightness temperature differences between the three water vapor channels of the MIR, and (c) the EDOP radar reflectivity along the flight track from 2217:30 to 2223:22 UTC on 25 January 1999 taken during the TRMM LBA campaign.

Figure 2. Same as Figure 1 but for the flight track from 1813:24 to 1816:14 UTC on 10 February 1999.

Figure 3. (a) Classified GCE cloud model data with cloud tops above 10 km, (b) deep convective clouds and convective overshooting determined by criteria (1) and (2) using the simulated brightness temperatures, cirrus clouds and other clouds are same as in (a).

Figure 4. Quality measure C as a function of the threshold values T_D for deep convective cloud and T_O for convective overshooting at viewing angles from 5° to 60°.

Figure 5. The distributions of deep convective cloud fractions in the tropics. The red contours enclose regions with the averaged surface rainfall greater than 3 $\mathrm{mm\,day^{-1}}$ derived from the TRMM 3B43 rainfall product for comparison.

Figure 6. The distributions of the weighted convective overshooting fraction of deep convective cloud. The red contours enclose the sea surface temperature greater than 28° (from NOAA CDC).

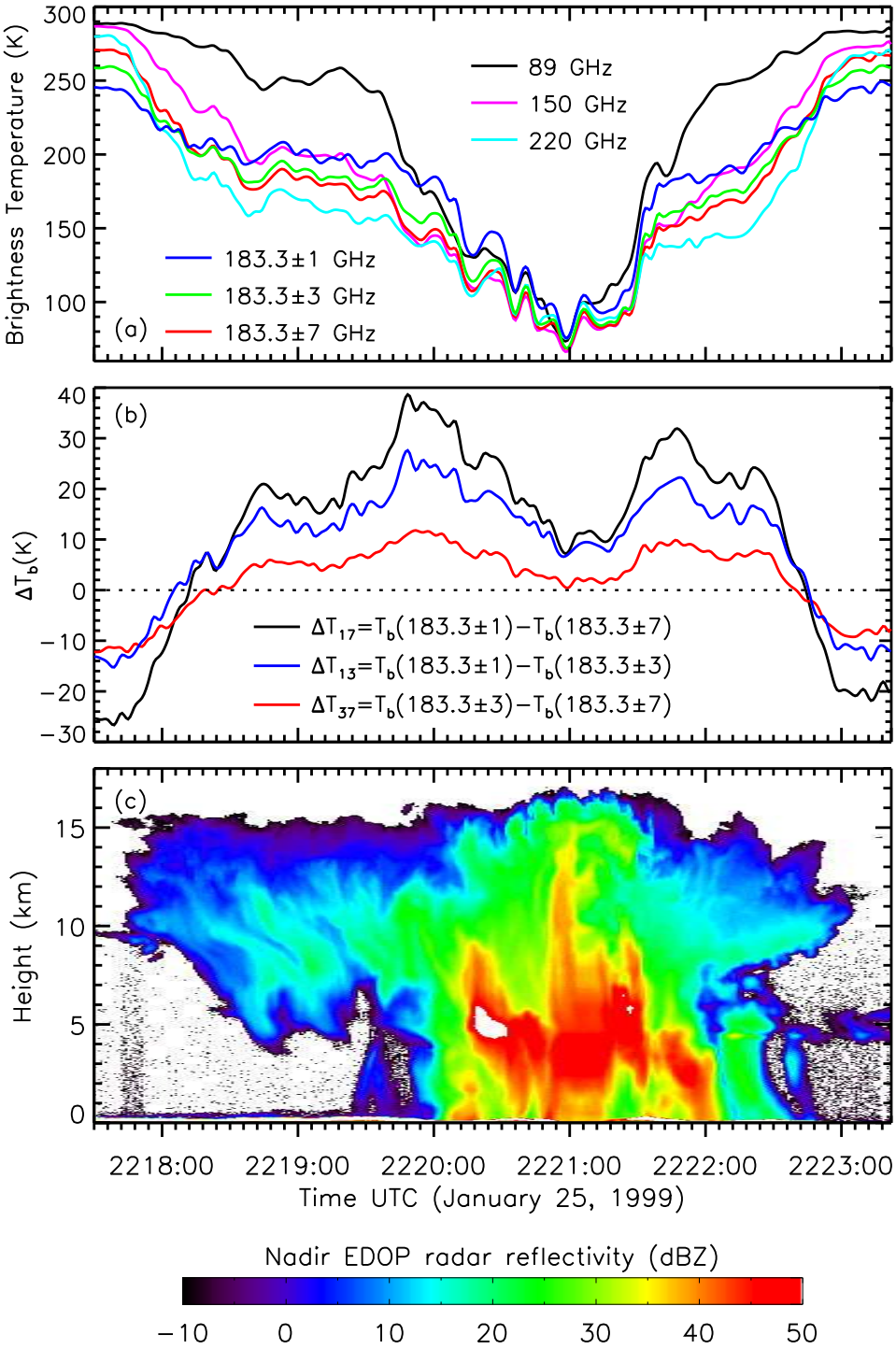

Figure 1. (a) The MIR brightness temperatures, (b) brightness temperature differences between the three water vapor channels of the MIR, and (c) the EDOP radar reflectivity along the flight track from 2217:30 to 2223:22 UTC on 25 January 1999 taken during the TRMM LBA campaign.

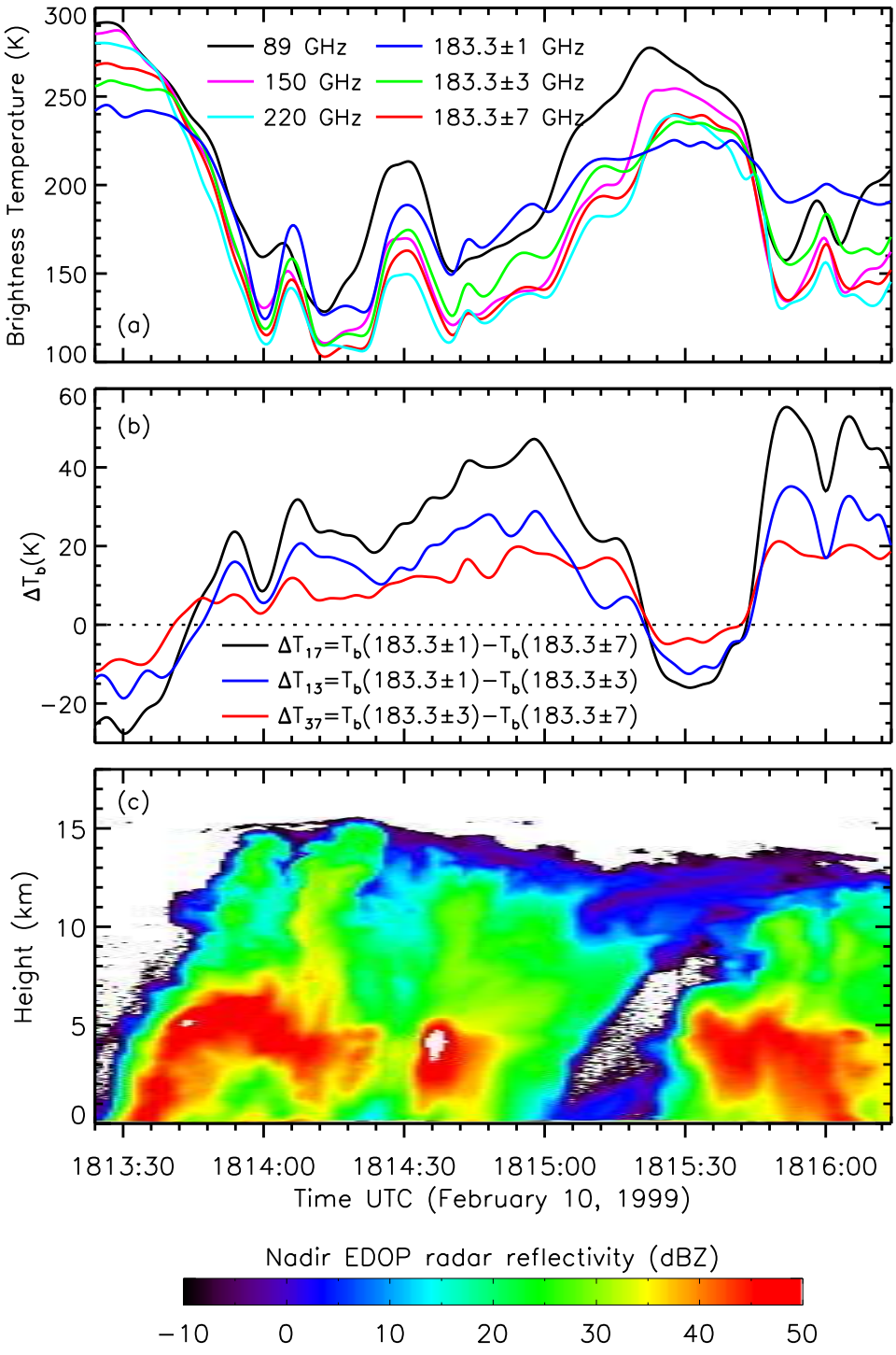

Figure 2. Same as Figure 1 but for the flight track from 1813:24 to 1816:14 UTC on 10 February 1999.

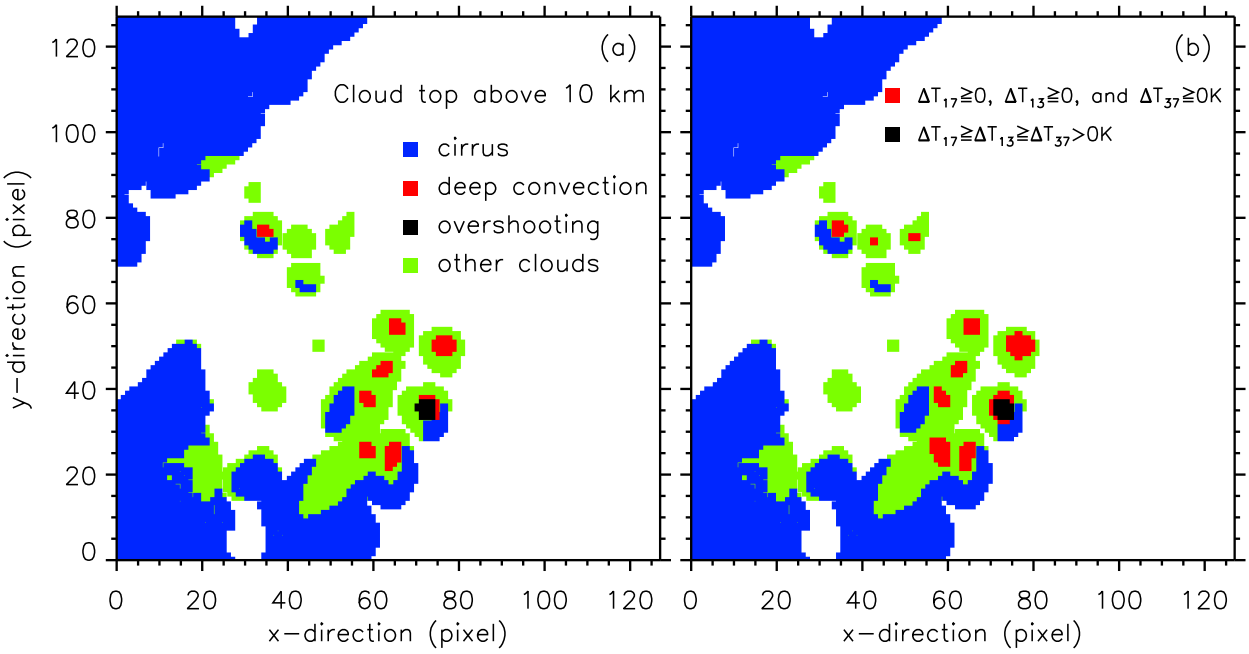

Figure 3. (a) Classified GCE cloud model data with cloud tops above 10 km, (b) deep convective clouds and convective overshooting determined by criteria (1) and (2) using the simulated brightness temperatures, cirrus clouds and other clouds are same as in (a).

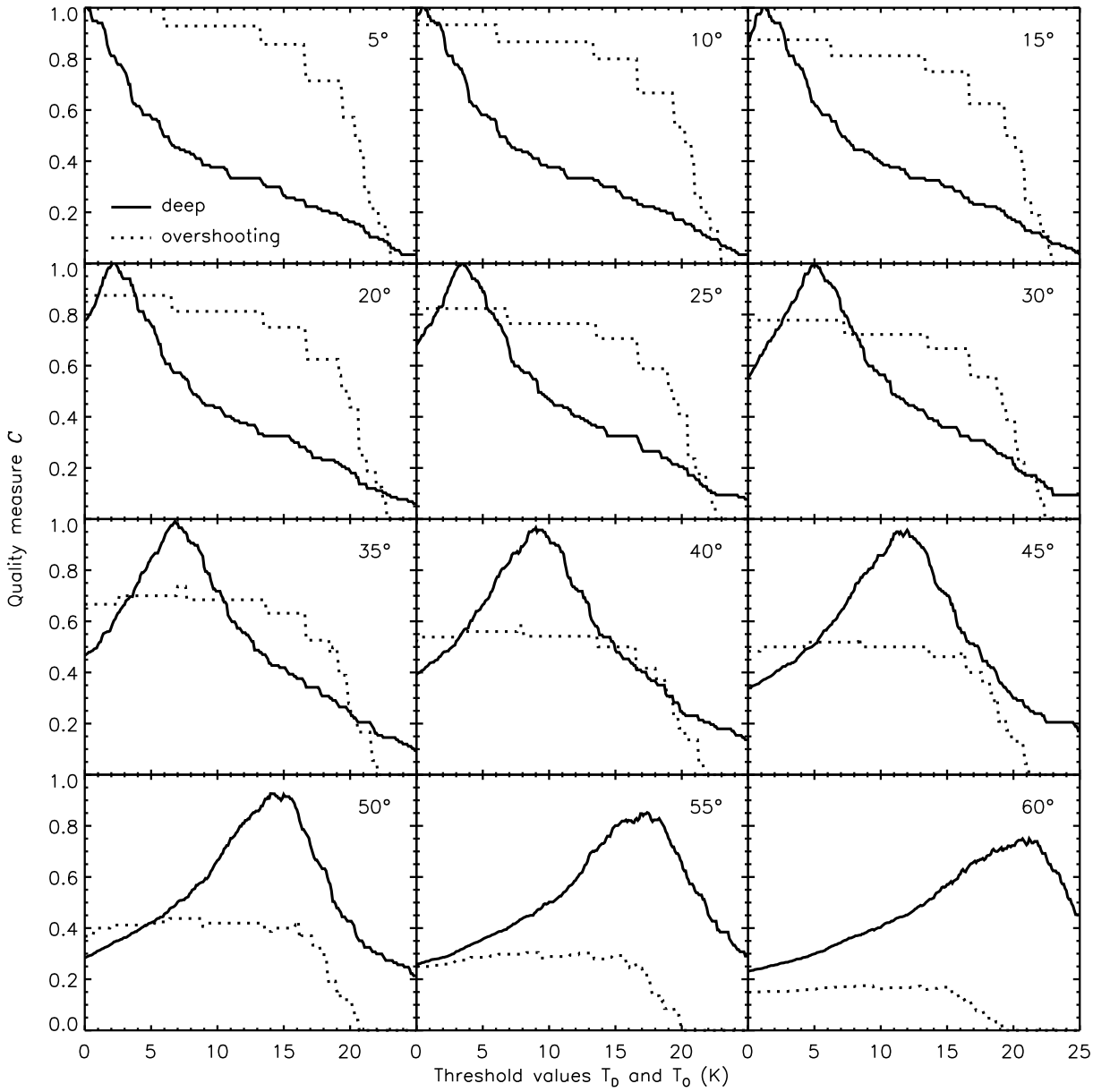

Figure 4. Quality measure C as a function of the threshold values T_D for deep convective cloud and T_O for convective overshooting at viewing angles from 5° to 60°.

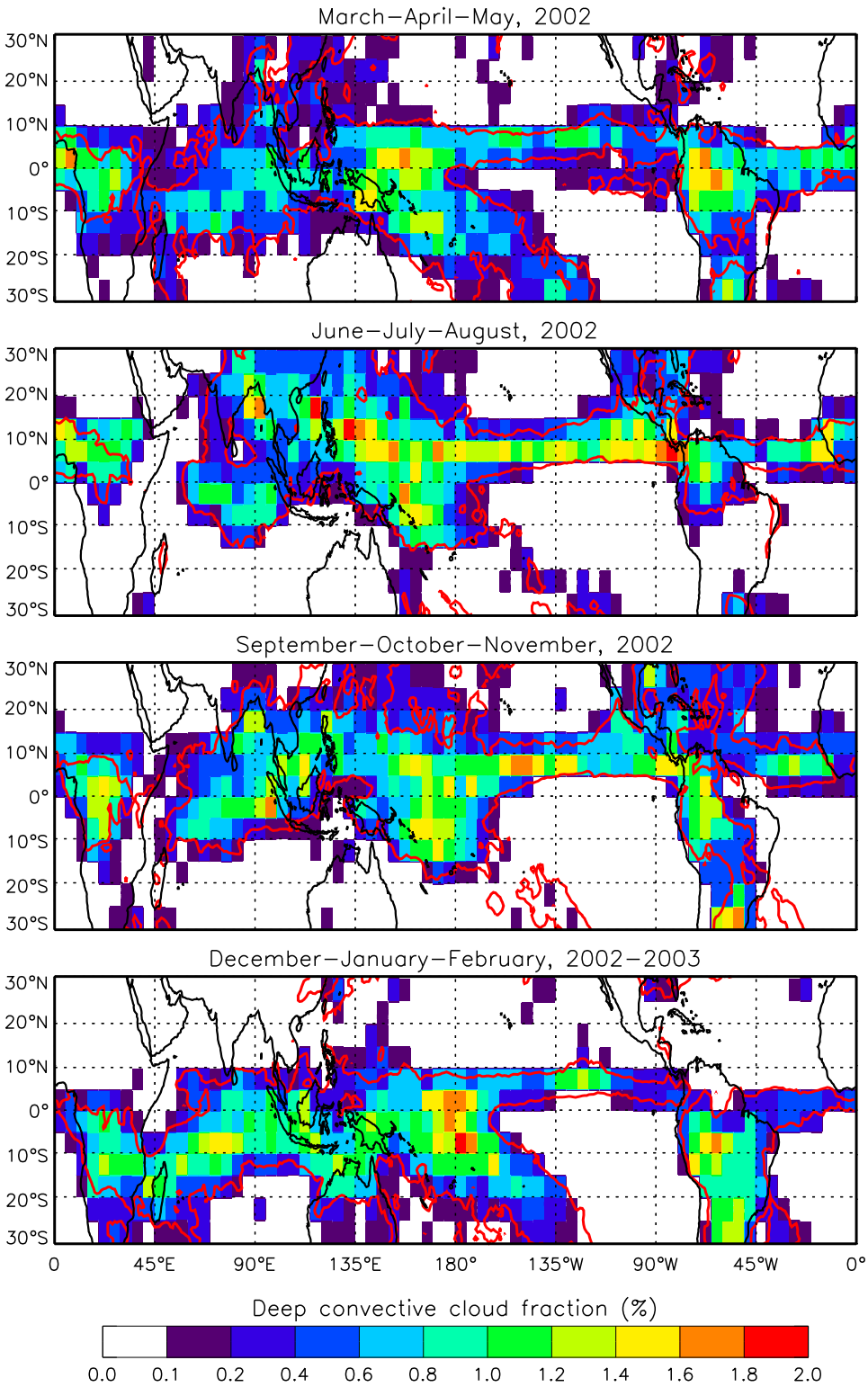

Figure 5. The distributions of deep convective cloud fractions in the tropics. The red contours enclose regions with the averaged surface rainfall greater than 3 mm day^{-1} derived from the TRMM 3B43 rainfall product for comparison.

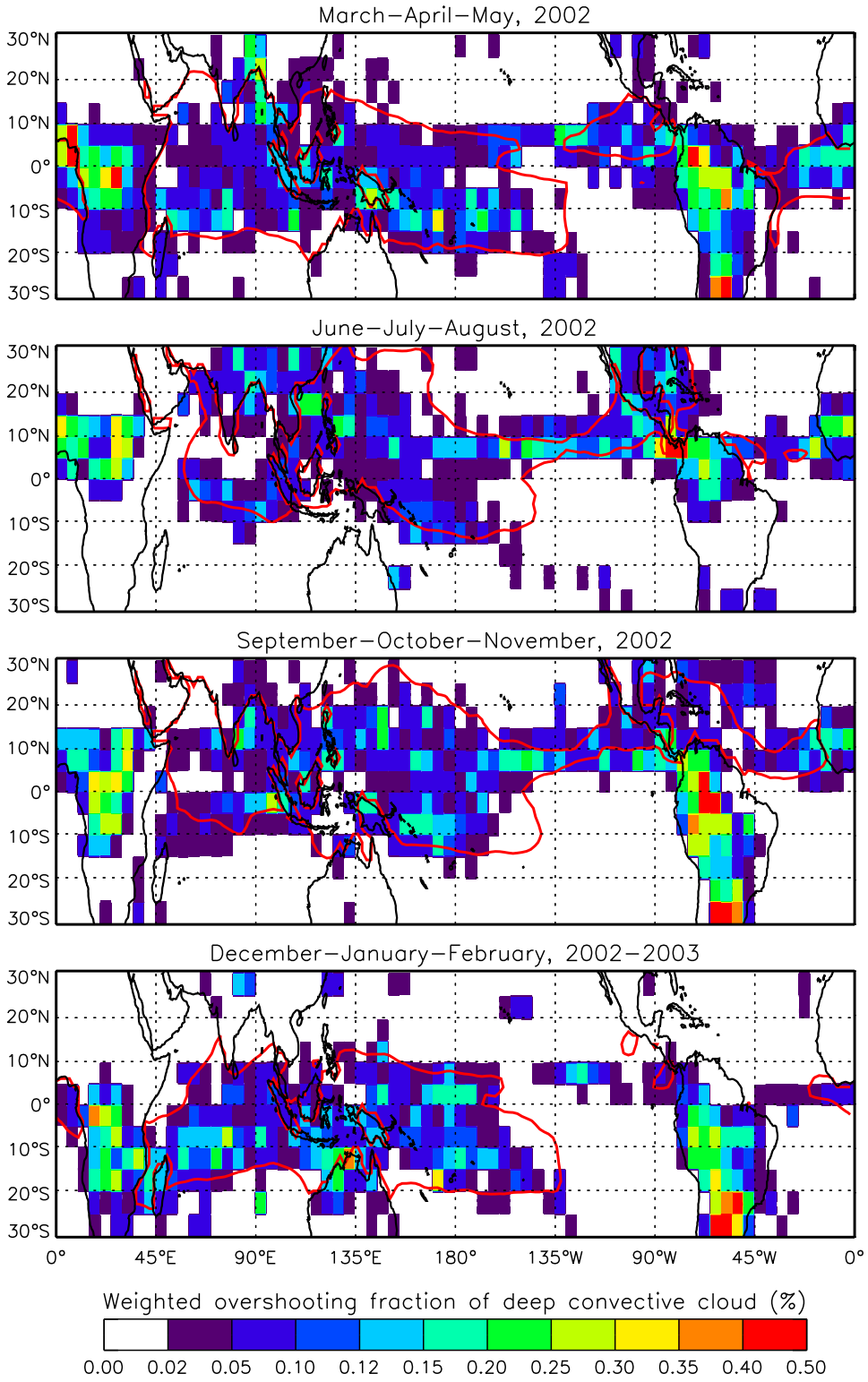

Figure 6. The distributions of the weighted convective overshooting fraction of deep convective cloud. The red contours enclose the sea surface temperature greater than 28° (from NOAA CDC).